JACS
JOURNAL OF THE AMERICAN CHEMICAL SOCIETY
Article
Cite This: J. Am. Chem. Soc. 2018, 140, 9730−9736
pubs.acs.org/JACS

Eu^{2+} Site Preferences in the Mixed Cation $K_2BaCa(PO_4)_2$ and Thermally Stable Luminescence

Jianwei Qiao,[†] Lixin Ning,[*,‡] Maxim S. Molokeev,[§,∥,⊥] Yu-Chun Chuang,[#] Quanlin Liu,[†] and Zhiguo Xia[*,†]

[†]The Beijing Municipal Key Laboratory of New Energy Materials and Technologies, School of Materials Sciences and Engineering, University of Science and Technology Beijing, Beijing 100083, P. R. China

[‡]Anhui Key Laboratory of Optoelectric Materials Science and Technology, Department of Physics, Anhui Normal University, Wuhu, Anhui 241000, P. R. China

[§]Laboratory of Crystal Physics, Kirensky Institute of Physics, Federal Research Center KSC SB RAS, Krasnoyarsk 660036, Russia

[∥]Siberian Federal University, Krasnoyarsk 660041, Russia

[⊥]Department of Physics, Far Eastern State Transport University, Khabarovsk 680021, Russia

[#]National Synchrotron Radiation Research Center, Hsinchu 300, Taiwan

Supporting Information

ABSTRACT: Site preferences of dopant Eu^{2+} on the locations of K^+, Ba^{2+}, and Ca^{2+} in the mixed cation phosphate $K_2BaCa(PO_4)_2$ (KBCP) are quantitatively analyzed via a combined experimental and theoretical method to develop a blue-emitting phosphor with thermally stable luminescence. Eu^{2+} ions are located at K2 (M2) and K3 (M3) sites of KBCP, with the latter occupation relatively more stable than the former, corresponding to emissions at 438 and 465 nm, respectively. KBCP:Eu^{2+} phosphor exhibits highly thermal stable luminescence even up to 200 °C, which is interpreted as due to a balance between thermal ionization and recombination of Eu^{2+} 5d excited-state centers with the involvement of electrons trapped at crystal defect levels. Our results can initiate more exploration of activator site engineering in phosphors and therefore allow predictive control of photoluminescence tuning and thermally stable luminescence for emerging applications in white LEDs.

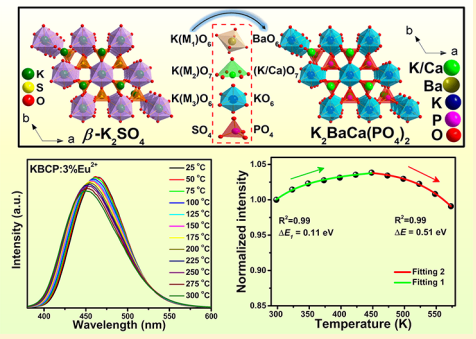

INTRODUCTION

Phosphor-converted white light-emitting diodes (pc-WLEDs) have been extensively considered as the most promising new generation solid state lighting sources due to their environmental friendliness, robustness, and long operation lifetimes.[1−4] Most commercially available pc-LEDs are based on $Y_3Al_5O_{12}:Ce^{3+}$ ($YAG:Ce^{3+}$) phosphors pumped by blue LEDs, which, however, suffer from poor color-rendering index (R_a < 75) and high correlated color temperatures (CCT > 4500 K) due to the lack of red components.[5] Near ultraviolet (NUV) LEDs assembled with blue, green, and red emitting phosphors have been exploited for their high quality white light emission with high color rendering property and superior color uniformity.[6,7] Nevertheless, thermal quenching (TQ) properties of phosphors seriously affects luminance efficiency and restricts their applications in pc-WLEDs, especially in high power conditions or laser LEDs.[8−10] Therefore, laboratory discovery of phosphors with high luminance and thermal stability is still an imperative challenge.

In terms of the currently used and available phosphors for pc-WLEDs, the number of blue emitting compounds is rather limited. Although the commercial blue emitting $BaMgAl_{10}O_{17}:Eu^{2+}$ and $Sr_3MgSi_2O_8:Eu^{2+}$ phosphors show a high luminance efficiency at room temperature, the TQ effect seriously reduce the emission intensity during the operation of LED.[11] Various techniques have been employed to minimize TQ, such as by using high structural rigidity phosphor, ceramic coating (SiO_2, TiO_2) over phosphors, and glass-ceramic phosphors.[12−17] In particular, it has been recently demonstrated that crystal defects may play a positive role in diminishing TQ of Eu^{2+} luminescence through a possible energy transfer from defect levels to the Eu^{2+} 5*d* levels owing to an increase of the Na disordering with increasing temperature in the $Na_3Sc_2(PO_4)_3:Eu^{2+}$ phosphor.[18] It is believed that the mixed cations in a host material could initiate the versatile site occupations of activators, and thus lead to the discovery of new phosphor systems, which is beneficial for optimization of luminescence properties toward practical applications.[19]

In recent years, our group has proposed a useful methodology for the discovery of new LED phosphors by mineral-inspired prototype evolution and new phase construction, which have been effectively applied to the discovery of new phosphors.[20−22] In addition, $ABPO_4:Eu^{2+}$ phosphors (A = Li,

Received: June 8, 2018
Published: July 9, 2018

DOI: 10.1021/jacs.8b06021
J. Am. Chem. Soc. 2018, 140, 9730−9736

Na, K, Rb; B = Ca, Sr, Ba) with β-K_2SO_4 type structure have been widely investigated due to their high thermal stability, such as $KSrPO_4:Eu^{2+}$, $KBaPO_4:Eu^{2+}$, and $RbBaPO_4:Eu^{2+}$.[23−25] Enlightened by the above reports, in the present work we successfully designed a novel blue-emitting phosphor $K_2BaCa(PO_4)_2:Eu^{2+}$ ($KBCP:Eu^{2+}$) from the β-K_2SO_4-type structure, which exhibits high luminescence thermal stability. Accordingly, the structural design principle, phase determination, Eu^{2+} site occupation and photoluminescence properties of $KBCP:Eu^{2+}$ phosphors are discussed in detail. Optimization of Eu^{2+} concentration revealed that the luminescence intensity of $KBCP:3\%Eu^{2+}$ exhibits zero TQ up to 200 °C. This behavior was explained as due to a balance between thermal ionization and recombination of Eu^{2+} 5d excited-state centers, involving the electrons trapped at crystal defect levels and transported through the host conduction band. This study may open up a new understanding and perspective for designing high thermal stability phosphors.

EXPERIMENTAL SECTION

Synthesis. A series of $KBCP:xEu^{2+}$ (x = 0−9%) were synthesized by the high temperature solid-state method. The stoichiometric mixtures of K_2CO_3 (A.R.), $BaCO_3$ (A.R.), $CaCO_3$(A.R.), $NH_4H_2PO_4$ (A.R.), and Eu_2O_3 (99.99%) were ground in an agate mortar and filled into an alumina crucible. Mixtures were sintered under a reducing atmosphere (5% H_2 /95% N_2) at 1200 °C for 4 h and then quenched to room temperature, and finely ground with a mortar for further characterization.

Characterization. Powder X-ray diffraction (XRD) measurements were performed on a D8 Advance diffractometer (Bruker Corporation, Germany) at 40 kV and 40 mA with Cu $K\alpha$ radiation (λ = 1.5406 Å). Synchrotron X-ray powder diffraction (SXRD) measurements were performed at TPS 09A (Taiwan Photon Source) of the National Synchrotron Radiation Research Center with a calibrated wavelength of 0.82656 Å. The powder sample was packed into a glass capillary. The one-dimensional powder diffraction patterns were recorded using MYTHEN 24K detector with 30 s exposure time. Rietveld structure refinements were conducted using TOPAS 4.2.[26] The morphology and microstructure of the samples were investigated using a scanning electron microscope (SEM, JEOL JSM-6510A). The photographs of microcrystal particle were obtained by a Nikon $LV_{100}ND$ optical microscope. The photoluminescence (PL), photoluminescence excitation (PLE) spectra and temperature dependent luminescence spectra were detected by a Hitachi F-4600 fluorescence spectrophotometer. The decay curve was collected by FLSP920 fluorescence spectrophotometer equipped with an nF900 flash lamp as the excitation source. Thermoluminescence (TL) spectra were recorded by using an FJ-427ALTL measuring instrument (Beijing Nuclear Instrument Factory) in the temperature range between 35 °C and 300 °C at a heating rate of 1 K s^{-1}. The quantum efficiency (QE) was measured using the FLS920 attached a barium sulfate coated integrating sphere, and a Xe900 lamp was used as an excitation source. The electroluminescence spectra, color-rendering index (R_a), and color temperature (CCT) of the as-fabricated W-LEDs were measured using a UV−vis−near IR spectro-photocolorimeter (PMS-80, Everfine).

COMPUTATIONAL METHODOLOGY

The $KBCP:Eu^{2+}$ crystals were modeled by 2 × 2 × 2 supercells containing 112 atoms, in which one of the $Ba^{2+}/K^+/Ca^{2+}$ ions was substituted by a Eu^{2+}. The nearest distance between Eu^{2+} ions in the periodic supercell systems is larger than 10.0 Å, which is large enough to avoid their mutual influence in view of the localized 4f electronic states of Eu^{2+}. Periodic DFT calculations were performed using the PBE+U approach with U = 2.5 eV for the Eu 4f electrons,[27,28] as implemented in the VASP code.[29,30] The $Ba(5s^25p^66s^2)$, $Ca(3p^64s^2)$, $K(3p^64s^1)$, $P(3s^23p^3)$, $O(2s^22p^4)$, and $Eu(5s^25p^64f^76s^2)$ were treated as valence electrons, and their interactions with the cores were described by the projected augmented wave (PAW) approach.[31] For the supercells with Eu^{2+} located at a K^+ site, the excess charge was compensated by introducing a uniform background charge density. The atomic structures of the supercells were fully optimized until the total energies and the forces on the atoms were converged to 10^{-6} eV and 0.01 eV $Å^{-1}$. For the calculation of thermodynamic charge transition levels of crystal defects, the PBE0 hybrid functional was employed,[32] as this functional has been shown to improve the results of the band gaps and defect properties in oxides when compared with pure PBE functional.[33] One k-point Γ was used to sample the Brillouin zone, and the cutoff energy of the plane-wave basis was set to 530 eV.

RESULTS AND DISCUSSION

Crystal Structure and Morphology. In β-K_2SO_4 type structures, there are three independent K cation sites (K(M1), K(M2) and K(M3)), which provides a generic platform to design new β-K_2SO_4 type compounds. As a representative, phosphates with the general formula $ABPO_4$ have been synthesized by the cosubstitution of $K^+ \rightarrow A^+$ (A = Li, Na, Rb, Cs), $K^+ \rightarrow B^{2+}$ (B = Ca, Sr, Ba, Mg, Zn), and $SO_4 \rightarrow PO_4$. Here, we successfully designed and synthesized a new $ABPO_4$ type phosphate $K_2BaCa(PO_4)_2$ through cosubstitution of $K(M1)O_6 \rightarrow BaO_6$, $K(M2)O_7 \rightarrow (K/Ca)O_7$, $K(M3)O_6 \rightarrow KO_6$, and $SO_4 \rightarrow PO_4$, as shown in Figure 1a. To characterize the structure of the material, Rietveld refinement of the powder XRD data was conducted (Figure 1b). All the peaks in the XRD pattern can be well indexed by trigonal cell (P-3m1) with parameters close to those for $NaBaPO_4$.[34] Therefore, $NaBaPO_4$ crystal structure was used as the starting model for Rietveld refinement. There are two Ba sites (M1 and M2 sites) in the $NaBaPO_4$ structure, with the M1 sites being fully occupied by Ba^{2+} ion and the M2 sites being occupied by 50% Ba^{2+} and 50% Na^+ ions. Additionally, $NaBaPO_4$ has one fully occupied Na site (M3 site). Our refinement showed that the M1 site in $K_2BaCa(PO_4)_2$ should be occupied by very heavy ion, but not for the M2 site. Thus, we suggest that, in $K_2BaCa(PO_4)_2$, Ba^{2+} and K^+ ions fully occupy the M1 and M3 sites, respectively, with the M2 sites being occupied by Ca^{2+} and K^+ ions. As for the Ca/K ratio at the M2 site, preliminary refinement showed that the M1 sites were fully occupied by Ba^{2+} ions without any traces of Ca^{2+} or K^+, and consequently the M2 sites should be occupied by 50% Ca^{2+} and 50% K^+ ions in accordance to the chemical formula $K_2BaCa(PO_4)_2$ (Figure S1 in the Supporting Information (SI)). Final refinement of this model was stable with low R-factors (Table S1, Figure 1b). Coordinates of atoms and main bond lengths are given in Tables S2 and S3, respectively. The crystallographic information file (CIF) of this new phase $K_2BaCa(PO_4)_2$ is also presented in the SI. Further details of the crystal structures $K_2BaCa(PO_4)_2$ may be obtained from Fachinformationszentrum Karlsruhe, 76344 Eggenstein-Leopoldshafen, Germany (fax: (+49)7247−808−666; e-mail: crystdata@fiz-karlsruhe.de; http://www.fiz-karlsruhe.de/request_for_deposited_data.html on quoting the deposition number CSD-434656.

To further determine which sites were occupied by Eu^{2+} ions, Rietveld refinement of high-quality synchrotron XRD data of $KBCP:9\%Eu^{2+}$ was conducted. There are three different sites which can be potentially occupied by Eu^{2+}:Ba

DOI: 10.1021/jacs.8b06021
J. Am. Chem. Soc. 2018, 140, 9730−9736

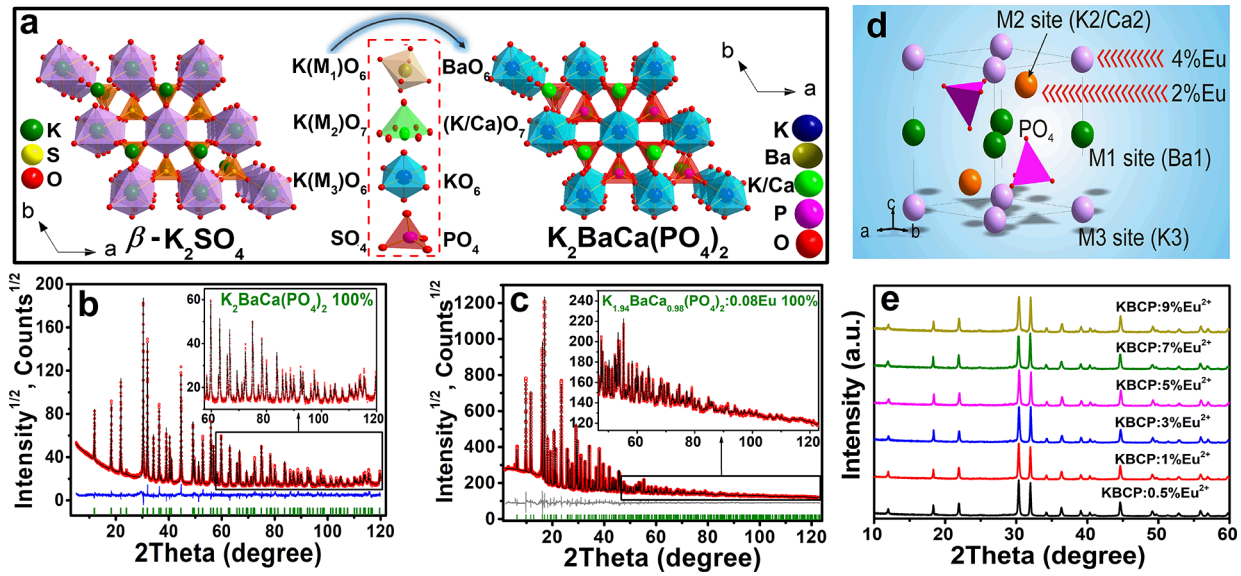

Figure 1. (a) Structural phase transformation model from β-K_2SO_4 prototype to new phase of KBCP via the different substitution construction on different cation sites. (b) XRD and (c) SXRD profile for Rietveld refinement result of KBCP and KBCP:9%Eu^{2+}, respectively. (d) Crystal structure of KBCP:9%Eu^{2+} and the occupied rates of Eu^{2+}. (e) XRD patterns of as-prepared KBCP:xEu^{2+} (x = 0.5−9%).

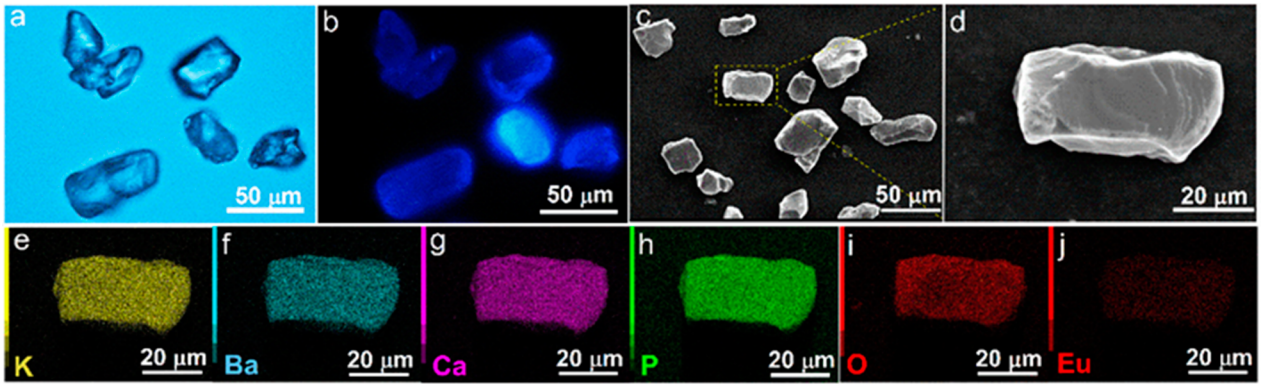

Figure 2. Optical microscope photographs of the KBCP: 3%Eu^{2+} microcrystal particles without (a) and with (b) 365 nm UV excitation. SEM images of the KBCP:Eu^{2+} microcrystal particles (c) and the enlarged single particle (d). EDS elemental mapping of the cross section of KBCP:3% Eu^{2+} for different elements (e−j).

(M1), Ca2/K2 (M2), and K3 (M3) sites (Figure S1). Eu occupations in all these sites were refined by taking into account that the sum of all ions occupancies in each site is equal to 1. The refinement was stable and gave low R-factors (Table S1, Figure 1d). Coordinates of atoms and main bond lengths are in Tables S2 and S3, respectively. Chemical formula from refinement was $K_{1.940(2)}BaCa_{0.980(2)}(PO_4)_2$:0.080(2)Eu and the obtained Eu doping level (8.0(2)%) is close to the suggested one (9%) during the preparation. Analysis of distribution over the host sites revealed that only M2 and M3 sites are occupied by Eu^{2+} (Table S2), and the amount at the latter sites is two times larger than that at the former sites (Figure 1d). The XRD patterns of as-obtained KBCP:xEu^{2+} ($0.5\% \leq x \leq 9\%$) are depicted in Figure 1e. The diffraction peaks of all samples are well matched with the trigonal (P-3m1) structure, which means that all samples are pure phase and doping Eu^{2+} ions do not cause significant changes to the crystal structure.

To characterize the morphology of KBCP:Eu^{2+} phosphors, optical microscope photographs, SEM, and EDS mapping were carried out. The optical microscope photographs of KBCP:Eu^{2+} particles without and with 365 nm UV light excitation are shown in Figure 2a, b, respectively. The bright blue light (Figure 2b) from the KBCP:Eu^{2+} microcrystals indicates that the phosphor may possess a high luminous efficiency. Figure 2c, d depict the SEM images of KBCP:Eu^{2+} microcrystals at different scales, and the smooth surfaces demonstrate that the microcrystals have a high degree of crystallinity. The elemental mapping images (Figure 2e−j) evidence that K, Ba, Ca, P, O, and Eu are very homogeneously dispersed within the phosphor particles. Moreover, both the optical microscopy and SEM images show that the particle morphology and the sizes of the as-prepared samples are very similar in the micrometer range, which benefits the fabrication for white LEDs devices.

Eu^{2+} Site Occupations by DFT. Eu^{2+} site occupations in mixed cations $K_2BaCa(PO_4)_2$ were also investigated by using DFT calculations. To do this, however, the occupation disorder of Ca/K at the M2 site needs to be properly modeled first. This was achieved by considering all possible configurations of Ca and K over the 16 M2 sites of a 2 × 2 × 2 supercell of $K_2BaCa(PO_4)_2$. With the occupancy ratio fixed at Ca/K = 1, there are in principle (16)!/(8! × 8!) = 12 870 different

DOI: 10.1021/jacs.8b06021
J. Am. Chem. Soc. 2018, 140, 9730−9736

configurations, which is extensive enough to explore any short-range order in their distribution. When the crystal symmetry of the supercell was taken into account with the method reported in ref 34,[35] the number of crystallographically distinct configurations necessary for calculations reduced to 204. Their relative occurrence probabilities P_m (m = 1, ..., 204) with multiplicities Ω_m were then evaluated by $P_m = \frac{1}{Z}\Omega_m \exp\left(-\frac{E_m}{kT}\right)$, where E_m is the DFT total energy, k is the Boltzmann constant, T (= 1473 K) is the synthesis temperature of the materials, and Z is the partition function. P_m comprises both the energetic and the multiplicity information, and can thus be used for direct comparison of independent configurations. DFT calculations revealed that that there are six inequivalent configurations constituting the major part of the total ensemble, with the occurrence probabilities P = 0.194, 0.134, 0.132, 0.092, 0.077, and 0.065, respectively. The probabilities for the other inequivalent configurations are each lower than 0.030. The undoped supercells with these six configurations were then employed to investigate Eu^{2+} site occupations at the host cationic sites.

The relative occupancies of Eu^{2+} at the K2 (M2) and K3 (M3) sites were first evaluated. In each of the above six undoped supercells, an Eu atom was substituted successively for the 16 K atoms (including eight K2 atoms and eight K3 atoms). From the calculated DFT total energies, the occurrence probability P_i of an Eu occupying a K2 or K3 site was calculated, by using $P_i = \frac{1}{Z_{tot}}\exp\left(-\frac{E_i}{kT}\right)$, ($i$ = 1, ..., 96), where E_i is the DFT total energy and Z_{tot} is the partition function. By summing the values of P_i for Eu^{2+} at the K2 and K3 sites, respectively, it was found the dopant Eu prefers to be at the K3 site over the K2 site, with the relative overall probabilities being 0.626 and 0.374, respectively. This is consistent with the Rietveld refinement result that the occupancy of Eu^{2+} at the K3 site is approximately two times larger than that at the K2 site.

Next, to investigate site preferences of Eu at the Ba1 (M1) and Ca2 (M2) sites relative to those at the K2 (M2) and K3 (M3) sites, the 2 × 2 × 2 undoped supercell with the most stable Ca2/K2 configuration (P = 0.194) was chosen for this investigation. The defect formation energies (E_f) were calculated for Eu_{Ba1}, Eu_{Ca2}, nearest-neighbor (NN) Eu_{K2}−(V_{K3}, K_{Ba}, or K_{Ca}), and NN Eu_{K3}−(V_{K2}, K_{Ba}, or K_{Ca}) substitutions. Detailed calculation procedure and results are given in the SI. The results show that Eu occupations at the Ba1 and Ca2 sites are energetically very unfavorable (by >2.5 eV in E_f) compared to the occupations at the K2 and K3 sites. It is thus expected that Eu^{2+} ions are mostly located at the K2 and K3 sites, consistent with experimental results. Additionally, it shows that for a given Eu_{K2} or Eu_{K3} substitution, the charge compensation by a NN V_K is much more stable than those by a NN K_{Ca} or K_{Ba}. It is worth noting that, although only one representative undoped supercell was employed to calculate the defect formation energies, the much higher E_f values of Eu_{Ba1} and Eu_{Ca2} than those of Eu_{K2} and Eu_{K3} ensures that the conclusion would not change if other undoped supercells were included for the investigation. Therefore, DFT calculations predict that most Eu^{2+} ions are located at K2 (M2) and K3 (M3) sites of KBCP, with the latter occupation relatively more stable than the former, supporting the results from Rietveld refinements.

Photoluminescence Properties. To evaluate photoluminescence properties of KBCP:Eu^{2+}, the PLE and PL spectra of the samples with different Eu^{2+} concentrations are measured and shown in Figure 3a. Under 350 nm UV excitation, the optimum emission was exhibited by the KBCP:3%Eu^{2+} sample.

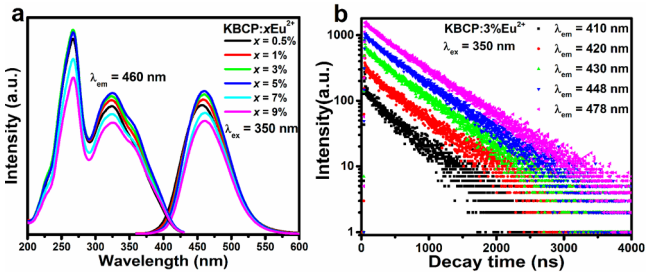

Figure 3. (a) PLE and PL spectra of KBCP:$x$$Eu^{2+}$ phosphors (x = 0.5–9%). (b) Decay curves of KBCP:3%Eu^{2+} emissions at wavelengths from 410 to 478 nm under 350 nm excitation at room temperature.

All the samples show a typical broad band emission corresponding to the 5d → 4f transition of Eu^{2+}, with the maximum emission wavelength at 460 nm. The broad emission band can be well decomposed into two Gaussian curves (Figure S2) peaking at 22 840 cm^{-1} (438 nm) and 21 482 cm^{-1} (465 nm), indicating the presence of two different Eu^{2+} luminescence centers, in agreement with the above results of Eu^{2+} site occupation from Rietveld refinements and DFT calculations. The emission with the higher (lower) intensity and maximum at 465 nm (438 nm) can be ascribed to Eu^{2+} at K3 (K2) sites, in view of the larger occupancy and smaller coordination polyhedron of Eu^{2+} at the K3 site than those at the K2 site. Figure 3a also shows the PLE spectra of KBCP:$x$$Eu^{2+}$ at room temperature, which display a typical two-band structure with band maxima at 265 and 327 nm, as a result of superposition of contributions from Eu^{2+} at the K2 and K3 sites.

The decay behaviors of Eu^{2+} emissions at wavelengths from 410 to 478 nm for KBCP:3%Eu^{2+} were measured and shown in Figure 3b. All the decay curves can be well fitted by a double-exponential function expressed as follows:

$$I = A_1\exp\left(-\frac{t}{\tau_1}\right) + A_2\exp\left(-\frac{t}{\tau_2}\right) \quad (1)$$

where I is the luminescence intensity, τ_1 and τ_2 are the fast and slow components of the decay time, and A_1 and A_2 are the corresponding fitting parameters. The fitting results are present in Table S4. It shows that each decay curve is dominated by the slow component, with the decay time in the range of 528–617 ns. The fast and slow components can be ascribed to Eu^{2+} located at K2 and K3 sites, respectively, in view of their relative occupancies by Eu^{2+}. The average lifetime gradually becomes longer with the increase of the monitored wavelength, as a result of the increasing contribution of the slow component corresponding to the emission of Eu^{2+} at K3 sites.

Zero-Thermal Quenching in KBCP:Eu^{2+} Phosphor. As one of critical factor to evaluate the potential of a new phosphor used for LEDs, the TQ behaviors of the representative KBCP:x%Eu^{2+} (x = 1%, 3%, 5%) samples were measured. Figure 4a illustrates the temperature-dependent emission spectra of KBCP:3%Eu^{2+} from 25 to 300 °C. Under 350 nm excitation, a slight blue-shift of the emission was observed with the increase of temperature. Similar observations were made for KBCP:$x$$Eu^{2+}$ with x = 1% and 5% (Figure S3). This could be due to the different sensitivities to temperature of Eu^{2+} emission at the K2 and K3 sites, i.e., the emission intensity of

DOI: 10.1021/jacs.8b06021
J. Am. Chem. Soc. 2018, 140, 9730–9736

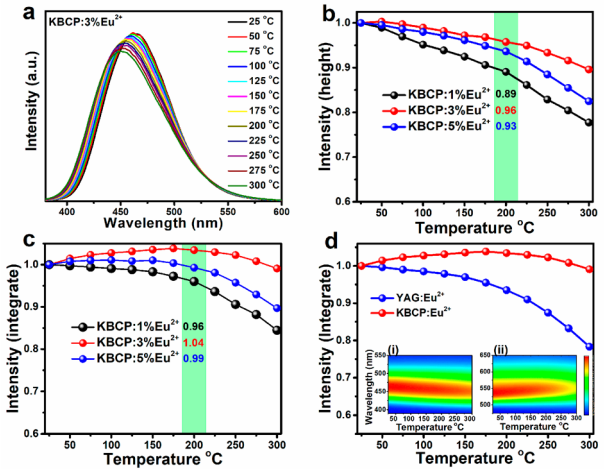

Figure 4. (a) Emission spectra of the KBCP:3%Eu^{2+} sample in the temperature range from 25 °C to 300 °C. Temperature-dependent normalized emission spectra of KBCP:$x$$Eu^{2+}$ (x = 1%, 3%, 5%) in terms of emission height (b) and area (c) excited at 350 nm. (d) Temperature-dependent normalized emission spectra of KBCP:3%Eu^{2+} in comparison with those of the commercial YAG:Ce^{3+} phosphor.

Eu^{2+} at K3 sites decreases slightly faster than that at K2 sites with increasing temperature.

Figure 4b, c shows respectively the temperature dependences of the peak and integrated intensities of Eu^{2+} emissions in KBCP:$x$$Eu^{2+}$ (x = 1%, 3%, and 5%) under 350 nm excitation. From Figure 4b, one sees that the peak intensities of all samples decrease continuously with increasing temperature, among which the peak intensity of KBCP:3%Eu^{2+} at 200 °C remains 96% of the intensity at 25 °C. By contrast, the integrated intensity of KBCP:$x$$Eu^{2+}$ decreases more slowly with the increase of temperature (Figure 4c), and the intensities of all samples at 200 °C remain >95% of that at 25 °C. In addition, the emission intensity shows a high stability when monitored continuously for 90 min at 100°C, 150°C, and 200°C, respectively (Figure S4). The different temperature-dependent behaviors of the peak and integrated emission intensities may be attributed to the emission band broadening with increasing temperature. In particular, the KBCP:3%Eu^{2+} sample exhibits a zero TQ up to a temperature of 275 °C. For comparison, the temperature dependence of the emission intensity of commercial LED phosphor YAG:Ce^{3+} were also collected under 455 nm excitation. As shown in Figure 4d, YAG:Ce^{3+} shows about 7% emission loss at 200 °C of the room temperature value, whereas KBCP:3%Eu^{2+} phosphor exhibits zero emission loss. When temperature increases from 25 to 300 °C, a minimal blue shift (Figure 4i) and red shift (Figure 4ii) are observed for KBCP:Eu^{2+} and YAG:Ce^{3+}, respectively. The remarkable thermal quenching behavior indicates that KBCP:Eu^{2+} is desirable for WLED applications.

Mechanism of Zero-Thermal Quenching. The temperature dependence of the integrated emission intensity of Eu^{2+}-activated phosphors is usually described by the empirical Arrhenius equation,[36] which implies that the intensity decreases with increasing T, and thus cannot explain the initial rise phase in the TQ behavior of KBCP:3%Eu^{2+} (Figure 4c, d). Recent studies showed that the zero TQ could be associated with the interaction between Eu^{2+} and crystal defects which act as electron-trapping centers.[18] As such, we performed TL measurements of KBCP:3%Eu^{2+}, and the result is displayed in Figure 5a. It shows a broad TL glow curve in the range from 30 °C to 200 °C, indicating a continuous distribution of trap

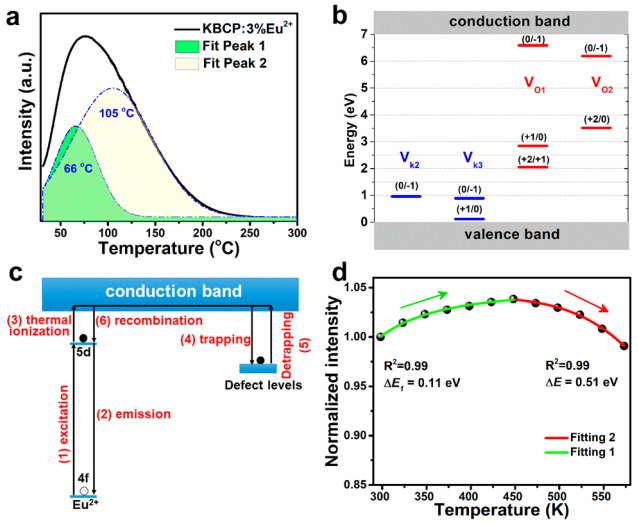

Figure 5. (a) TL curve and its deconvolutions of KBCP:3%Eu^{2+}. (b) Schematic representation of calculated thermodynamic charge transition levels for $V_{K2,3}$ and $V_{O1,2}$ in KBCP using the DFT-PBE0 method. (c) A simplified model to describe the initial rise of the integrated emission intensity with increasing temperature in KBCP:3%Eu^{2+}. (d) Nonlinear fitting of the thermal quenching behavior of KBCP:3%Eu^{2+} by two different equations.

depths. By fitting the TL curve with two Gaussian bands peaking at 66 °C and 105 °C, the characteristic trap depths (E_T) were estimated to be 0.68 and 0.76 eV by using the crude relationship $E_T = T/500$ eV, where the temperature T is in units of kelvin (K).[37]

The crystal defects associated with the trap depths could be either potassium vacancies (V_K) which act as the main charge compensators for the excess charge of Eu_K substitutions, or oxygen vacancies (V_O) which are present due to the reducing conditions during preparation of the materials. To clarify the nature of the defects that could be involved in the zero TQ, thermodynamic charge transition levels of V_{K2}, V_{K3}, V_{O1}, and V_{O2} were calculated by using hybrid DFT with PBE0 functional. The charge transition level indicates the Fermi level at which the formation energies of a defect in two charge states are equal.[33,38,39] The undoped KBCP supercell with the most stable Ca2/K2 configuration was chosen for this investigation. The results are listed in Table S5, and are also schematically depicted in Figure 5b. It shows that $V_{O1,2}$ ($V_{K2,3}$) can behave as trapping centers of electrons (holes) from the conduction (valence) band. In particular, the $\varepsilon(0/-)$ levels of V_{O1} and V_{O2}, which are related to trapping of an electron by a neutral V_O and changing its charge state to −1, are predicted to be 0.42 and 0.82 eV below the bottom of the conduction band. These values are closed to the characteristic trap depths (0.68 and 0.76 eV) as estimated from TL measurements. Therefore, we suppose that the defects involved in the initial rise phase of zero thermal quenching are most likely due to oxygen vacancies in the host material.

Since the net charges of Eu_K and V_O are of the same sign, the two single defects are expected to be far from each other for electrostatic reasons, and thus the conduction band states should be involved in the electron transport between them if it happens. With this in mind, the initial rise of integrated

DOI: 10.1021/jacs.8b06021
J. Am. Chem. Soc. 2018, 140, 9730−9736

intensity with increasing temperature as observed in the thermal quenching behavior of KBCP:3%Eu^{2+} may be explained by a simplified model as schematically shown in Figure 5c. For the steady state luminescence at a given temperature, there is a balance between thermal ionization of Eu^{2+} 5d electrons into the host conduction band followed by trapping of electrons at defect levels [processes (3) and (4)] and detrapping of electrons at defect levels followed by recombination with Eu^{3+} to yield excited Eu^{2+} 5d centers [processes (5) and (6)]. By using rate equations to model the processes, the following simple expression for the dependence of the emission intensity (I) on temperature (T) can be derived (see SI-2 for details):

$$I(T) = \frac{I_0}{1 + A\exp(\Delta E_1/kT)} \quad (2)$$

where I_0 is a parameter representing the emission intensity at $T = \infty$ K, A is a constant, and $\Delta E_1 = E_{trap} - E_{5d}$ where E_{trap} (E_{5d}) is the energy separation between the defect level (Eu^{2+} 5d level) and the bottom of the host conduction band. If E_{trap} is larger than E_{5d}, then the above expression implies that $I(T)$ increases with increasing T. A good fitting of the expression to the thermal quenching behavior of KBCP:3%Eu^{2+} in the range of T = 298−448 K is exhibited in Figure 5d. Thus, the initial rise of the emission intensity with increasing T is most likely due to the fact that an increase of thermal energy is beneficial for the recombination process in comparison with the trapping process. With further increase of temperature, other nonradiative decay processes become increasingly important (e.g., through crossover between the 4f ground and 5d excited levels or other channels to return to the 4f ground state), and start dominating the temperature-dependent behavior of the emission intensity. Hence the intensity starts to drop with increasing temperature, which may be described by the conventional Arrhenius eq (Figure 5d):

$$I(T) = \frac{I_0}{1 + A\exp(-\Delta E/kT)} \quad (3)$$

where I_0 and I_T are the initial emission intensities of the phosphor at T = 0 K and experimental temperature, respectively, A is a constant, ΔE is the activation energy, and k is the Boltzmann constant. The calculated ΔE is 0.51 eV, which is quite high to ensure a small emission loss with the increase of temperature.[40] It is important to realize that in the above simplified model to explain the initial rise phase of TQ behavior of KBCP:3%Eu^{2+}, the larger value of trap depth (E_{trap}) than that of the energy separation (E_{5d}) between the Eu^{2+} 5d level and the bottom of the conduction band is a crucial condition. For KBCP:1%Eu^{2+} and KBCP:5%Eu^{2+}, this might not be the case, or other nonradiative decay processes are dominant already in the initial phase, as manifested by the thermal quenching behaviors of the samples.

CIE Chromaticity Coordinates and Application for WLEDs. The CIE chromaticity coordinates of KBCP:3%Eu^{2+} phosphor are shown in Figure 6a. KBCP:Eu^{2+} appears as a homogeneous powder and shows bright blue light with the CIE coordinate of (0.142, 0.116). Under 350 nm excitation, the internal quantum efficiency KBCP:3%Eu^{2+} is 83% via a statistical average value at room temperature, and the measurement method and calculation details of the internal quantum efficiency are shown in Figure S5. Finally, pc-WLED was fabricated by combining a 365 nm near-UV LED chip with the mixture of blue (KBCP:Eu^{2+}), commercial green (Ba_2SiO_4:Eu^{2+}) and red ($CaAlSiN_3$:Eu^{2+}) phosphors, as presented in Figure 6b. The CCT, R_a value and the CIE coordinate of the as obtained WLED is 5326 K, 85 and (0.328, 0.338), respectively. These results demonstrate that KBCP:Eu^{2+} has potential to serve as blue-emitting phosphor for pc-WLED.

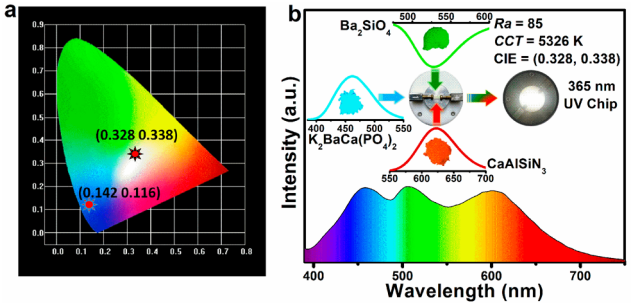

Figure 6. (a) CIE color coordinates of KBCP:3%Eu^{2+} and the fabricated WLED. (b) Photograph and electroluminescent spectrum of WLED fabricated by blue (KBCP:Eu^{2+}), green (Ba_2SiO_4:Eu^{2+}), and red ($CaAlSiN_3$:Eu^{2+}) phosphors driven by a UV chip (λ_{max} = 365 nm).

CONCLUSIONS

In summary, we have successfully developed a new blue-emitting KBCP:Eu^{2+} phosphor from the β-K_2SO_4 type structure with thermally stable luminescence. The refinement analysis of XRD patterns and DFT calculation support that Eu^{2+} occupied the K2 (M2) and K3 (M3) cationic sites of KBCP. It was proposed that the competition between thermal ionization and recombination of Eu^{2+} 5d excited-state centers led to the high thermal stability of luminescence in KBCP:Eu^{2+}. The fabricated WLED with a blending of commercial green (Ba_2SiO_4:Eu^{2+}) and red ($CaAlSiN_3$:Eu^{2+}) phosphors gives a high CRI (R_a = 85) demonstrating the potential for near-UV white LEDs. The concept of exploiting substitution of activator in the mixed cation host is expected to open the gateway for developing phosphors with thermally stable luminescence.

ASSOCIATED CONTENT

Supporting Information

The Supporting Information is available free of charge on the ACS Publications website at DOI: 10.1021/jacs.8b06021.

Figures S1−S5 and Tables S1−S5, as well as their corresponding notes, calculation details, and results for defect formation energies (DOCX)

Crystal structure of $K_2BaCa(PO_4)_2$ (CIF)

AUTHOR INFORMATION

Corresponding Authors

*ninglx@mail.ahnu.edu.cn

*xiazg@ustb.edu.cn

ORCID

Lixin Ning: 0000-0003-2311-568X

Maxim S. Molokeev: 0000-0002-8297-0945

Quanlin Liu: 0000-0003-3533-7140

Zhiguo Xia: 0000-0002-9670-3223

Notes

The authors declare no competing financial interest.

ACKNOWLEDGMENTS

This work is supported by the National Natural Science Foundation of China (No. 51722202, 91622125, 51572023,

DOI: 10.1021/jacs.8b06021
J. Am. Chem. Soc. 2018, 140, 9730−9736

and 11574003), Natural Science Foundations of Beijing (2172036) and M.M. acknowledges support of the Russian Foundation for Basic Research (17-52-53031).

REFERENCES

(1) Xia, Z. G.; Liu, Q. L. *Prog. Mater. Sci.* **2016**, *84*, 59−117.
(2) Qin, X.; Liu, X. W.; Huang, W.; Bettinelli, M.; Liu, X. G. *Chem. Rev.* **2017**, *117*, 4488−4527.
(3) Pust, P.; Weiler, V.; Hecht, C.; Tucks, A.; Wochnik, A. S.; Henss, A. K.; Wiechert, D.; Scheu, C.; Schmidt, P. J.; Schnick, W. *Nat. Mater.* **2014**, *13*, 891−896.
(4) Reineke, S. *Nat. Mater.* **2015**, *14*, 459−462.
(5) Wang, Z.; Ha, J.; Kim, Y. H.; Im, W. B.; McKittrick, J.; Ong, S. P. *Joule* **2018**, *2*, 914−926.
(6) Wei, Y.; Cao, L.; Lv, L. M.; Li, G. G.; Hao, J. R.; Gao, J. S.; Su, C. C.; Lin, C. C.; Jang, H. S.; Dang, P. P.; Lin, J. *Chem. Mater.* **2018**, *30*, 2389−2399.
(7) Wang, L.; Xie, R.-J.; Suehiro, T.; Takeda, T.; Hirosaki, N. *Chem. Rev.* **2018**, *118*, 1951−2009.
(8) Daicho, H.; Iwasaki, T.; Enomoto, K.; Sasaki, Y.; Maeno, Y.; Shinomiya, Y.; Aoyagi, S.; Nishibori, E.; Sakata, M.; Sawa, H.; Matsuishi, S.; Hosono, H. *Nat. Commun.* **2012**, *3*, 1132.
(9) Terraschke, H.; Wickleder, C. *Chem. Rev.* **2015**, *115*, 11352−11378.
(10) Zhu, H.; Lin, C. C.; Luo, W.; Shu, S.; Liu, Z.; Liu, Y.; Kong, J.; Ma, E.; Cao, Y.; Liu, R. S.; Chen, X. *Nat. Commun.* **2014**, *5*, 4312.
(11) Hermus, M.; Phan, P.-C.; Duke, A. C.; Brgoch, J. *Chem. Mater.* **2017**, *29*, 5267−5275.
(12) Im, W. B.; Brinkley, S.; Hu, J.; Mikhailovsky, A.; DenBaars, S. P.; Seshadri, R. *Chem. Mater.* **2010**, *22*, 2842−2849.
(13) Im, W. B.; George, N.; Kurzman, J.; Brinkley, S.; Mikhailovsky, A.; Hu, J.; Chmelka, B. F.; DenBaars, S. P.; Seshadri, R. *Adv. Mater.* **2011**, *23*, 2300−2305.
(14) Fan, X. T.; Chen, W. B.; Xin, S. Y.; Liu, Z. C.; Zhou, M.; Yu, X.; Zhou, D. C.; Xu, X. H.; Qiu, J. B. *J. Mater. Chem. C* **2018**, *6*, 2978−2982.
(15) Zhang, X.; Wang, J.; Huang, L.; Pan, F.; Chen, Y.; Lei, B.; Peng, M.; Wu, M. *ACS Appl. Mater. Interfaces* **2015**, *7*, 10044−10054.
(16) Lee, H. S.; Yoo, J. W. *Appl. Surf. Sci.* **2011**, *257*, 8355−8359.
(17) Zhuang, J. Q.; Xia, Z. G.; Liu, H. K.; Zhang, Z. P.; Liao, L. B. *Appl. Surf. Sci.* **2011**, *257*, 4350−4353.
(18) Kim, Y. H.; Arunkumar, P.; Kim, B. Y.; Unithrattil, S.; Kim, E.; Moon, S. H.; Hyun, J. Y.; Kim, K. H.; Lee, D.; Lee, J. S.; Im, W. B. *Nat. Mater.* **2017**, *16*, 543−550.
(19) Shi, R.; Wang, X.; Huang, Y.; Tao, Y.; Zheng, L.; Liang, H. *J. Phys. Chem. C* **2018**, *122*, 7421−7431.
(20) Chen, M. Y.; Xia, Z. G.; Molokeev, M. S.; Wang, T.; Liu, Q. L. *Chem. Mater.* **2017**, *29*, 1430−1438.
(21) Xia, Z.; Liu, G.; Wen, J.; Mei, Z.; Balasubramanian, M.; Molokeev, M. S.; Peng, L.; Gu, L.; Miller, D. J.; Liu, Q.; Poeppelmeier, K. R. *J. Am. Chem. Soc.* **2016**, *138*, 1158−1161.
(22) Xia, Z. G.; Xu, Z. H.; Chen, M. Y.; Liu, Q. L. *Dalton Trans.* **2016**, *45*, 11214−11232.
(23) Zhang, S.; Nakai, Y.; Tsuboi, T.; Huang, Y.; Seo, H. J. *Inorg. Chem.* **2011**, *50*, 2897−2904.
(24) Song, H. J.; Yim, D. K.; Roh, H.-S.; Cho, I. S.; Kim, S.-J.; Jin, Y.-H.; Shim, H.-W.; Kim, D.-W.; Hong, K. S. *J. Mater. Chem. C* **2013**, *1*, 500−505.
(25) Lin, C. C.; Xiao, Z. R.; Guo, G.-Y.; Chan, T.-S.; Liu, R.-S. *J. Am. Chem. Soc.* **2010**, *132*, 3020−3028.
(26) *TOPAS V.2: General profile and structure analysis software for powder diffraction data—User's Manual*; Bruker AXS: Karlsruhe, Germany, 2008.
(27) Dudarev, S.; Botton, G.; Savrasov, S.; Humphreys, C.; Sutton, A. *Phys. Rev. B: Condens. Matter Mater. Phys.* **1998**, *57*, 1505−1509.
(28) Chaudhry, A.; Boutchko, R.; Chourou, S.; Zhang, G.; Grønbech-Jensen, N.; Canning, A. *Phys. Rev. B: Condens. Matter Mater. Phys.* **2014**, *89*, 155105.
(29) Kresse, G.; Furthmüller, J. *Phys. Rev. B: Condens. Matter Mater. Phys.* **1996**, *54*, 11169−11186.
(30) Kresse, G.; Joubert, D. *Phys. Rev. B: Condens. Matter Mater. Phys.* **1999**, *59*, 1758−1775.
(31) Blöchl, P. E. *Phys. Rev. B: Condens. Matter Mater. Phys.* **1994**, *50*, 17953−17979.
(32) Perdew, J. P.; Ernzerhof, M.; Burke, K. *J. Chem. Phys.* **1996**, *105*, 9982−9985.
(33) Freysoldt, C.; Grabowski, B.; Hickel, T.; Neugebauer, J.; Kresse, G.; Janotti, A.; Van de Walle, C. G. *Rev. Mod. Phys.* **2014**, *86*, 253−305.
(34) Launay, S.; Mahe, P.; Quarton, M. *Mater. Res. Bull.* **1992**, *27*, 1347−1353.
(35) Grau-Crespo, R.; Hamad, S.; Catlow, C. R. A.; Leeuw, N. H. d. *J. Phys.: Condens. Matter* **2007**, *19*, 256201.
(36) Bhushan, S.; Chukichev, M. *J. Mater. Sci. Lett.* **1988**, *7*, 319−321.
(37) Van den Eeckhout, K.; Smet, P. F.; Poelman, D. *Materials* **2010**, *3*, 2536−2566.
(38) Ning, L.; Cheng, W.; Zhou, C.; Duan, C.; Zhang, Y. *J. Phys. Chem. C* **2014**, *118*, 19940−19947.
(39) Shi, H.; Du, M. H. *Phys. Rev. B: Condens. Matter Mater. Phys.* **2014**, *90*, 174103.
(40) Chen, M. Y.; Xia, Z. G.; Molokeev, M. S.; Lin, C. C.; Su, C. C.; Chuang, Y.-C.; Liu, Q. L. *Chem. Mater.* **2017**, *29*, 7563−7570.

DOI: 10.1021/jacs.8b06021
J. Am. Chem. Soc. 2018, 140, 9730−9736